Multichannel and high dimensional integrated photonic quantum memory

Zhong-Wen Ou, 1,2,3,* Tian-Xiang Zhu, 1,2,3,* Peng-Jun Liang, 1,2,3,4 Xiao-Min Hu, 1,2,3,4 Zong-Quan Zhou, 1,2,3,4,† Chuan-Feng Li, 1,2,3,4 and Guang-Can Guo 1,2,3,4

¹Laboratory of Quantum Information, University of Science and Technology of China, Hefei 230026, China

²Anhui Province Key Laboratory of Quantum Network,

University of Science and Technology of China, Hefei 230026, China

³CAS Center For Excellence in Quantum Information and Quantum Physics,

University of Science and Technology of China, Hefei 230026, China

⁴Hefei National Laboratory, University of Science and Technology of China, Hefei 230026, China

Integrated photonic quantum memories are essential components for scalable quantum networks and photonic information processors. However, prior implementations have been confined to single-channel operation, limiting their capacity to manipulate multiple photonic pulses and support high-dimensional information. In this work, we introduce an 11-channel integrated quantum memory based on laser-written waveguide arrays in $^{151}{\rm Eu}^{3+}:{\rm Y}_2{\rm SiO}_5$ crystals. On-chip electrode arrays enable independent control over the readout times for each channel via Stark-shift-induced atomic interference. Our device achieves random-access quantum storage of three time-bin qubits with a fidelity exceeding 99%, as well as storage of five-dimensional path-encoded quantum states with a fidelity above 96%. This multichannel integrated storage device enables versatile applications through its random access capability and lays a solid foundation for the development of high-dimensional quantum networks in integrated architectures.

INTRODUCTION

Quantum memories for light, which can faithfully store and retrieve a stream of photonic pulses, are essential components for large-scale quantum networks [1–4] and photonic information processing [5–11]. Integrated operations of such photonic memories are vital for achieving low power consumption and compact device size, which are necessary for scalable applications. Storage of photonic qubits in integrated quantum memories have been successfully demonstrated using various fabrication techniques in rare-earth-ion-doped solids [12–15], achieving high efficiencies [16], long storage times [17], wide bandwidth and large multimode capacities [12, 15, 18]. However, these devices have been limited to single-channel operation, while the most intriguing advantage of integrated devices—multichannel operations within a single device—has been absent until now, hindering their capabilities in active manipulating multiple photonic pulses. Moreover, high-dimensional photonic quantum states (qudits) have been proven to be indispensable for quantum communication and quantum computing [19– 23], as they can carry more information in a single photon. However, existing integrated photonic memories are incapable of storing photonic qudits due to the challenge of encoding high-dimensional information within a singlechannel integrated structure.

Here, we present an 11-channel integrated photonic quantum memory based on laser-written waveguide arrays fabricated in an $^{151}\mathrm{Eu}^{3+}$:Y₂SiO₅ crystal, which is integrated with coplanar electrode arrays for active electric control. All channels are independently controlled and phase coherent, allowing for the random-access storage [24–26] of multiple time-bin qubits and reliable storage of

high-dimensional photonic qudits, laying the foundation for flxible applications in photonic information processing [6, 9] and high-dimensional quantum networks [20].

RESULTS

Experimental setup. A microscopic image of the multichannel integrated quantum memory is depicted in Fig. 1(b). The substrate is a 0.07% doped ¹⁵¹Eu³⁺:Y₂SiO₅ crystal, a unique material that enables coherent light storage for 1 hour [27]. The substrate dimensions are $5\times4\times15$ mm along the crystal's $D1\times D2\times b$ axes. Eleven depressed cladding optical waveguides [28] are fabricated along the b aixs using a femtosecond laser micromachining (FLM) system. Electrode arrays are plated on the crystal's $D2 \times b$ surface to individually apply electric fields to the Eu³⁺ ions within the optical waveguides, allowing active control of the storage process. Further details about the device are provided in Sec. 1 of Supplemental Materials. We employ a pair of acoustic optical deflectors (AODs) to individually address the eleven memory channels (Fig. 1(a)). By applying controlled radio-frequency (RF) signals to the AODs, light can be programmatically directed to any single memory channel or their coherent superposition.

The storage of photons is achieved using the Stark-modulated atomic frequency comb (SMAFC) protocol [28–30], which absorbs single photons via an atomic frequency comb (AFC) [31, 32] and enables on-demand retrieval in discrete steps through active control of the atomic rephasing process by Stark-induced interference between two subgroups of atoms. Specifically, with an AFC prepared with a frequency periodicity of Δ , an elec-

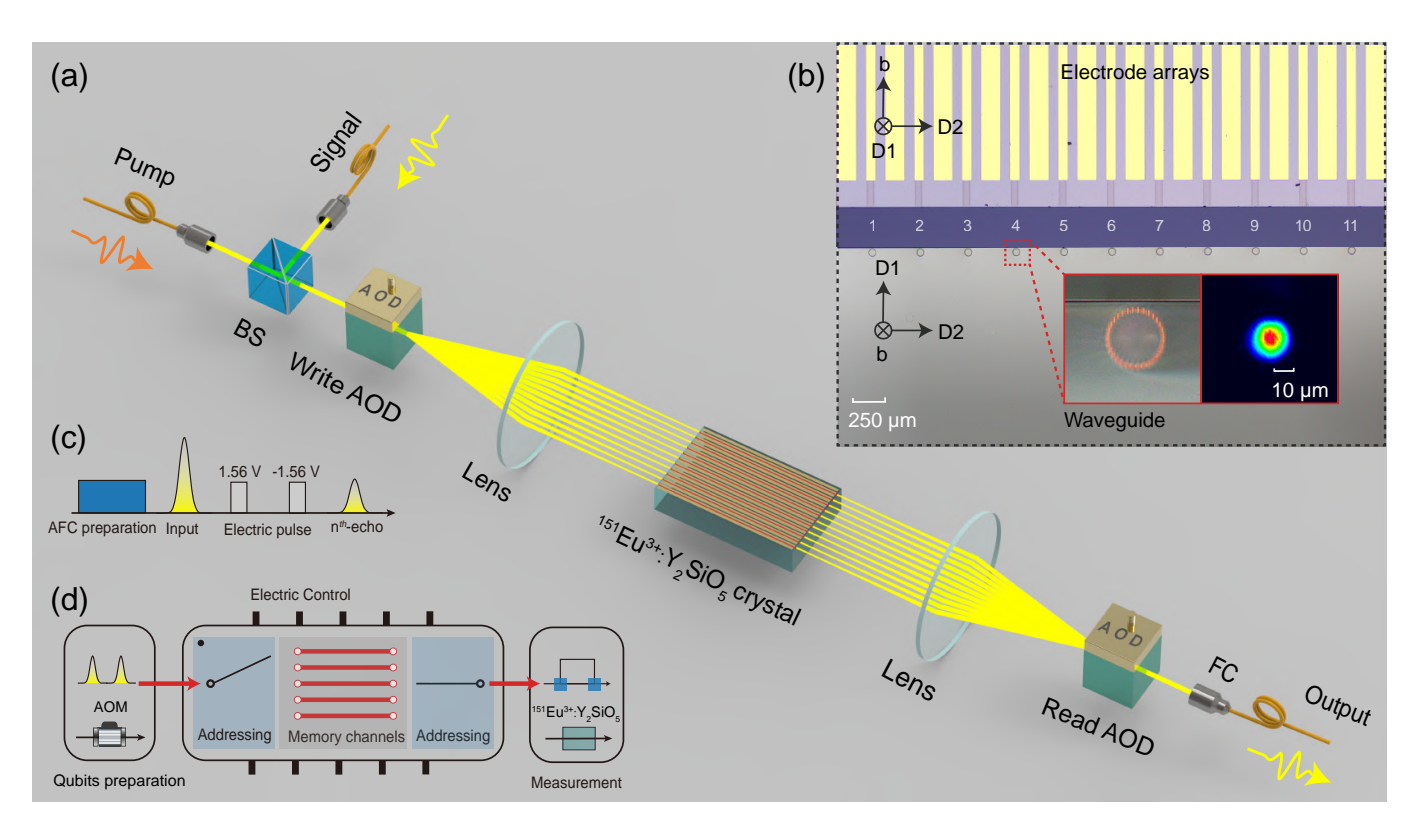


FIG. 1. Experimental setup. (a) Schematic of main optical setup. The pump beam and the signal beam are combined via a 90:10 (R:T) beam splitter (BS). The combined beam is addressed to 11 memory channels based on optical waveguide array through the write acoustic optical deflector (AOD) and a lens. The optical polarization is aligned parallel to the crystal's D1 axis. The read AOD couples the output from 11 channels into a single-mode fiber via a fiber collimator (FC) for further single-photon analysis. (b) Microscopic view of waveguide arrays and electrode arrays. The upper picture is a vertical view of the device, showing center electrodes with a width of $50~\mu m$ used to apply the electrical pulse, and neighboring electrodes with a width of $100~\mu m$ that are grounded. The lower image is a front view of the device, with small circles indicating the cross-section of each waveguide. Inset (red box): Enlarged view of the waveguide and the mode profile. (c) Time sequence for SMAFC storage. The n^{th} AFC echo can be on-demand retrieved from the memory by applying a pair of electric field pulses. (d) The time-bin qubit storage architecture consists of a qubit generation unit (prepared via an acousto-optic modulator, AOM), a memmory unit with electric control, and a measurement unit (analyzed using another $n^{151}Eu^{3+}$:Y₂SiO₅ crystal prepared with AFC).

tric field pulse applied during the time interval $[0,1/\Delta]$ can suppress the standard AFC echo emission at $1/\Delta$ through complete destructive interference. A second electric field pulse with the opposite polarity applied during the time interval $[(n-1)/\Delta, n/\Delta]$ can then read out the photons at $t=n/\Delta$, corresponding to the n^{th} AFC echo. The timing sequence for the SMAFC storage process is illustrated in Fig. 1(c). An electric pulse with a duration of 50 ns and a voltage of 1.56 V is sufficient for our integrated device, allowing for easy control using standard electronic devices. Fig. 1(d) depicts the time-bin qubit storage architecture, which allows multiple qubits to be stored and retrieved in any desired order.

Multichannel storage of single-photon-level inputs. We first demonstrate multiplexed storage with eleven independent channels. The inputs are weak coherent pulses with a mean photon number per pulse of $\mu =$ 0.14. We set $\Delta = 2$ MHz for all channels. Each channel allows on-demand retrieval controlled by corresponding electric pulses (Fig. 2(a)). The average storage efficiency for the $1^{st}/2^{nd}$ AFC echo is $39.2 \pm 0.2\%/31.3 \pm 0.2\%$, The average storage efficiency for the $1^{st}/2^{nd}$ AFC echo is $39.2\pm0.2\%/31.3\pm0.2\%$, surpassing the previous record of 27.8% for integrated photonic memories [30], with consistent storage performance across all 11 channels. Our device further features inter-channel crosstalk below -40 dB and electrical crosstalk-induced efficiency degradation below 1% (see Sec. 2 in Supplemental Materials), making it well-suited for implementing more complex manipulations across many independent storage channels.

Random access storage of multiple time-bin qubits. Static-access multiplexing has been thoroughly investigated in solid-state quantum memories [15, 33–35], where trains of photonic pulses are absorbed and retrieved in a rigid, first-in-first-out order. By contrast, our multichannel memory—each channel equipped with fully

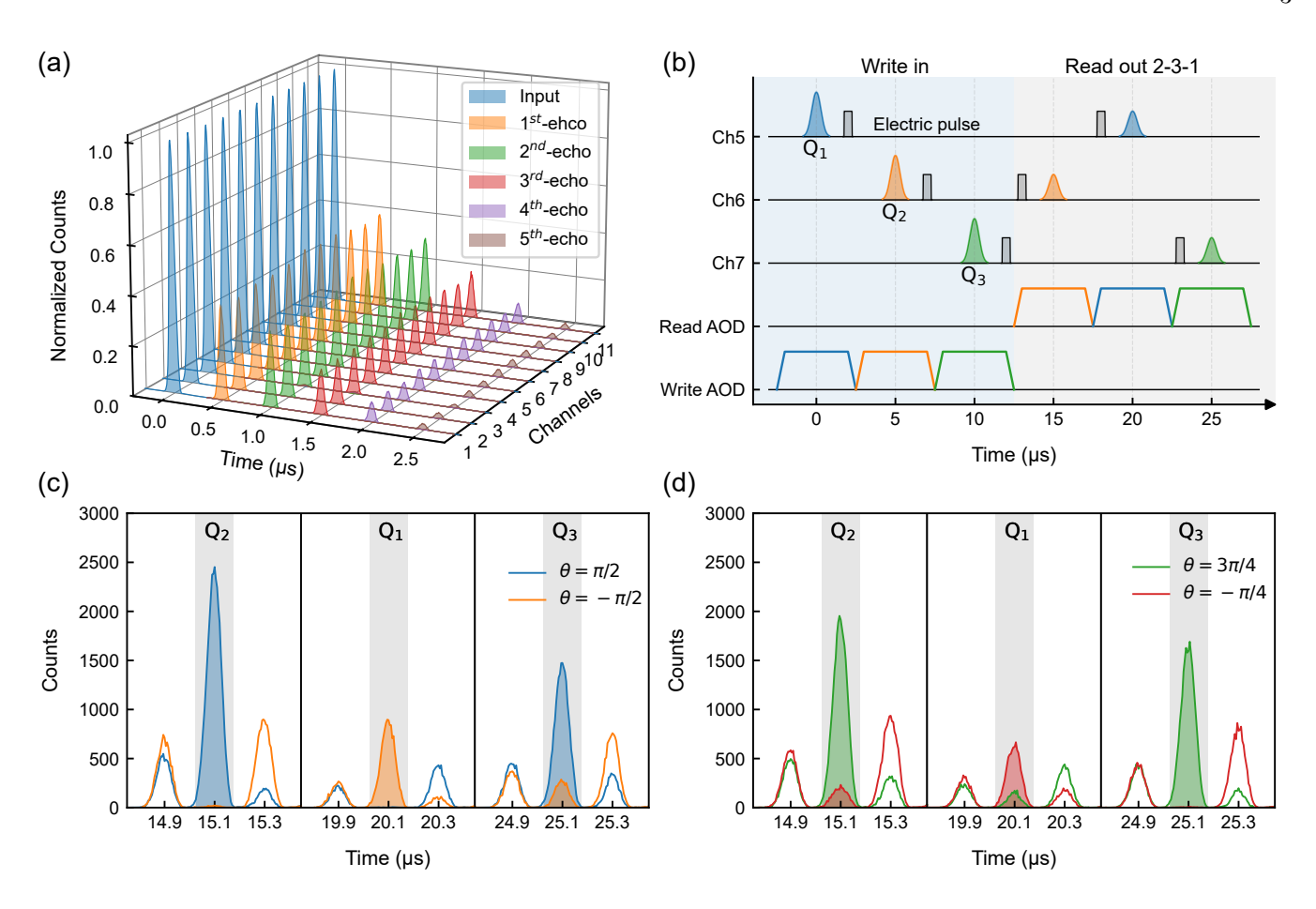


FIG. 2. Multiplexed and random access quantum storage of time-bin qubits. (a) Photon counting histograms for multiplexed storage of weak coherent inputs, demonstrating balanced efficiency for all 11 channels. On-demand retrieval of each channel is independently controlled via the corresponding electrodes, enabling precise and flexible operation. (b) The time sequence for random access quantum storage of three time-bin qubits is illustrated. The colors of the pulses represent distinct RF frequencies associated with the corresponding memory channels. The shown sequence exemplifies a specific retrieval order of 2-1-3, which can be reconfigured by adjusting the timing of the second electric pulses per channel, enabling arbitrary read-out orders. (c,d) Interference measurements on the retrieved time-bin qubits are presented for the read-out order of 2-3-1. The results correspond to input qubits $Q_1: (|e\rangle - i|l\rangle)/\sqrt{2}$, $Q_2: (|e\rangle + i|l\rangle)/\sqrt{2}$ and $Q_3: (|e\rangle + e^{i3\pi/4}|l\rangle)/\sqrt{2}$, with the readout basis defined as $(|e\rangle + e^{i\theta}|l\rangle)/\sqrt{2}$. (c) The read-out phases are set to $\theta = \pi/2$ (blue solid line) and $\theta = -\pi/2$ (orange solid line). (d) The read-out phases are set to $\theta = 3\pi/4$ (green solid line) and $\theta = -\pi/4$ (red solid line). The interference visibilities measured for Q_2 , Q_1 , and Q_3 within a 150-ns detection window are $98.5 \pm 0.1\%$, $99.3 \pm 0.1\%$, and $99.3 \pm 0.1\%$, respectively.

independent electrical control—breaks this constraint, allowing any stored temporal mode to be retrieved on demand, in any sequence. This functionality defines random-access quantum memory (RAQM) [24–26], a versatile resource for multiplexed quantum repeaters [36] and advanced photonic information processing [5].

We begin by initializing memory channels 5, 6, and 7 through the simultaneous preparation of AFC structures, with a comb spacing of 200 kHz. Subsequently, the write AOD sequentially writes the time-bin qubits Q_1 , Q_2 and Q_3 into memory channels 5, 6, and 7, respectively. Finally, these three qubits can be read out in any desired order, as illustrated in Fig. 2(b), by controlling the timing of the electric pulses applied to each channel and the read AOD. Here we show an example to store distinct

time-bin qubits $Q_1:(|e\rangle-i|l\rangle)/\sqrt{2}$, $Q_2:(|e\rangle+i|l\rangle)/\sqrt{2}$ and $Q_3:(|e\rangle+e^{i3\pi/4}|l\rangle)/\sqrt{2}$, where $|e\rangle$ and $|l\rangle$ represent the early and the late qubits, respectively, separated by an interval of 200 ns. To analyze the superposition states, we employ another $^{151}\mathrm{Eu^{3+}}:Y_2\mathrm{SiO_5}$ crystal, prepared with an AFC structure, to serve as an unbalanced Mach–Zehnder interferometer [37]. The AFC storage time is set to 200 ns to match with the time-bin interval and the interference phase is controlled by the AFC detuning (see Methods for details). The fidelity of superposition states is defined as F=(V+1)/2, while V is the interference visibility [30, 38, 39]. Example interference results for Q_1,Q_2 and Q_3 are shown in Fig. 2(c) with readout phases $\theta=\pi$ $(-\pi)$, and in Fig. 2(d) with readout phases $\theta=3\pi/4$ $(-\pi/4)$, giving a readout order

of 2-1-3. Additionally, we measured the readout fidelity for the orders 1-2-3, 2-1-3, and 3-2-1, as summarized in Table I. All measured fidelities exceeded 99%, demonstrating the high reliability of the random access storage process. In our current demonstration, the number of random-access storage channels is primarily constrained by the storage time and the relatively slow rise time of the AOD (1.9 μ s). The integrated spin-wave quantum storage, as demonstrated in our recent work [17], can significantly extend both the storage time and the number of accessible channels.

TABLE I. Storage fidelity of time-bin qubits $Q_1:(|e\rangle-i|l\rangle)/\sqrt{2}$, $Q_2:(|e\rangle+i|l\rangle)/\sqrt{2}$ and $Q_3:(|e\rangle+e^{i3\pi/4}|l\rangle)/\sqrt{2}$ with readout arranged in various orders.

Order	F_{Q_1}	F_{Q_2}	F_{Q_3}
-	$99.6 \pm 0.1\%$		
2 - 1 - 3	$99.3\pm0.1\%$	$99.7\pm0.1\%$	$99.6 \pm 0.1\%$
3-2-1	$99.4\pm0.2\%$	$99.7\pm0.1\%$	$99.1\pm0.1\%$

Quantum storage of high-dimensional spatial states. High-dimensional quantum information (qudits) [20] has emerged as an indispensable resource in quantum networks, offering several advantages. These include higher information capacity [40] with increased resistance to noise [41] in quantum communication, and the ability to simplify quantum logic [23] while enhancing fault tolerance [22] in quantum computing. However, previous implementations of integrated photonic quantum memories have been limited to the storage of two-dimensional information [12–17], primarily focusing on time-bin-encoded qubits. Our multichannel integrated quantum memory overcomes this limitation, providing an ideal platform for the storage of path-encoded high-dimensional quantum states.

In our experiments, photons can be coherently encoded into or projected onto d-dimensional path-encoded quantum states $|\psi\rangle = \sum_{n=1}^d a_n |C_n\rangle$, where C_n denotes the memory channel n and $a_n \in \mathbb{C}$ represents the complex superposition coefficient. These coefficients are precisely controlled through adjusting the amplitudes and phases of the RF signals driving AODs [42, 43]. As shown in Fig. 3(a), interference fringes for distinct input states demonstrate preserved inter-path coherence, with phase control implemented through RF phase adjustments to the read AOD. To perform four-dimensional quantum storage, we select channels 5, 6, 7, and 8 to prepare an AFC structure with a comb spacing of 2 MHz. The input states are $|\psi_{in}\rangle = |C_n\rangle, (|C_n\rangle + |C_m\rangle)/\sqrt{2}, \text{ and } (|C_n\rangle + i|C_m\rangle)/\sqrt{2},$ with mean photon number $\mu = 0.98$ per pulse, where $5 \le n < m \le 8$. For the 2^{nd} SMAFC echo retrieved at 1 µs, we perform four-dimensional quantum state tomography (QST) using the bases: $|C_n\rangle$, $(|C_n\rangle + |C_m\rangle)/\sqrt{2}$, and $(|C_n\rangle + i|C_m\rangle)/\sqrt{2}$, where $5 \le n < m \le 8$. As an example, Fig. 3(b) displays the reconstructed density

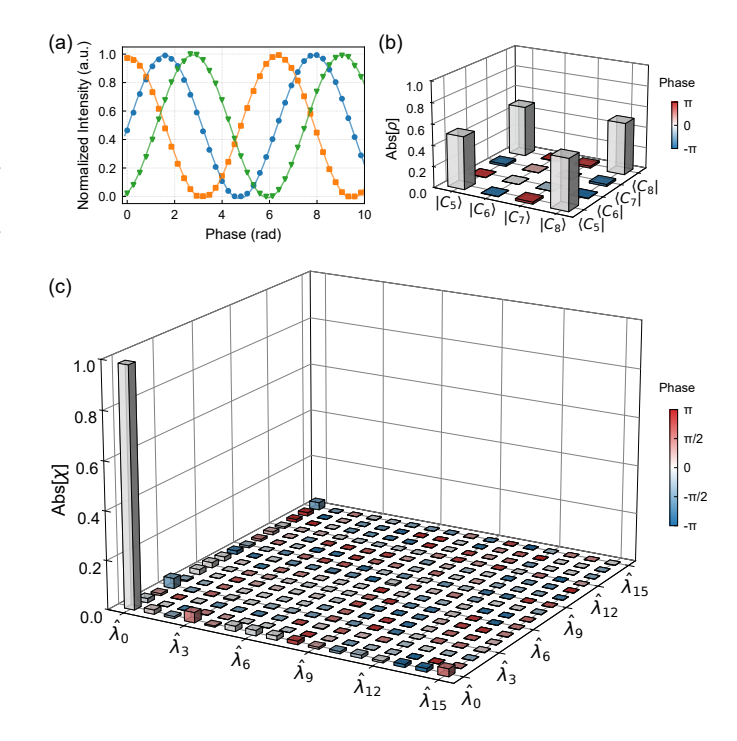


FIG. 3. Integrated quantum memory for four-dimensional path-encoded quantum information. (a) Interference fringes measured for three example input states: $(|C_6\rangle + |C_7\rangle)/\sqrt{2}$ (blue circles), $(|C_6\rangle + i|C_7\rangle)/\sqrt{2}$ (orange squares) and $(|C_7\rangle + |C_8\rangle)/\sqrt{2}$ (green triangles). Data points are fitted with cosine functions (solid lines). (b) The reconstructed density matrix for input state $(|C_5\rangle + |C_8\rangle)/\sqrt{2}$ is shown, with a measured fidelity of $98.5 \pm 0.6\%$. (c) The reconstructed process matrix χ for four-dimensional quantum storage is presented. The basis operators include $\hat{\lambda}_0 = I_{4\times 4}$, the identify operator, and $\hat{\lambda}_i$, $(1 \le i \le 15)$, which are the generators of the SU(4) group. For (b) and (c), the height of the bar indicates the absolute value of the matrix elements, while the color represents the phase.

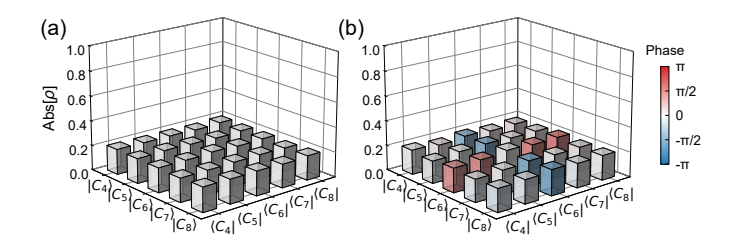


FIG. 4. Integrated quantum memory for five-dimensional quantum states. The reconstructed density matrix for outputs with inputs of $|\psi_1\rangle = (|C_5\rangle + |C_6\rangle + |C_7\rangle + |C_8\rangle + |C_9\rangle)/\sqrt{5}$ (a) and $|\psi_2\rangle = (|C_5\rangle + |C_6\rangle + i|C_7\rangle + |C_8\rangle + |C_9\rangle)/\sqrt{5}$ (b), with measured fidelities of 97.9±0.5% and 96.1±0.5%, respectively. The height of the bar represents the absolute value of matrix elements while the color denotes the phase.

matrix of the retrieved state when the input is prepared as $(|C_5\rangle + |C_8\rangle)/\sqrt{2}$. To fully characterize the multichannel memory performance for four-dimensional storage, we implement four-dimensional quantum process tomogra-

phy (QPT) [44] (see Sec. 7 in Supplemental Materials). The reconstructed process matrix χ shown in Fig. 3(c) demonstrates a process fidelity of $F_{\chi}=97.9\pm0.2\%$ with respect to the identity operator. Based on QPT and optimization algorithms (see Sec. 8 in Supplemental Materials), we show that our device achieves a quantum channel capacity of $C=1.932\pm0.007$, well above the single-qubit limit (C=1) and providing unambiguous evidence for the benefit of high-dimensional storage.

We further demonstrate five-dimensional quantum state storage using path-superposition states $|\psi_1\rangle =$ $(|C_5\rangle + |C_6\rangle + |C_7\rangle + |C_8\rangle + |C_9\rangle)/\sqrt{5}$ and $|\psi_2\rangle = (|C_5\rangle +$ $|C_6\rangle + i|C_7\rangle + |C_8\rangle + |C_9\rangle /\sqrt{5}$ encoded across channels 5, 6, 7, 8, and 9, with an input intensity of $\mu = 0.38$. The measured storage efficiencies for states $|\psi_1\rangle$ and $|\psi_2\rangle$ are $30.2 \pm 0.3\%$ and $31.4 \pm 0.4\%$, respectively, for the 2^{nd} SMAFC echo retrieved at 1 µs. We perform quantum state tomography on the readout using the complete measurement basis set $\{|C_n\rangle, (|C_n\rangle + |C_m\rangle)/\sqrt{2}, (|C_n\rangle +$ $i|C_m\rangle/\sqrt{2}$, $(5 \le n < m \le 9)$. The reconstructed density matrices ρ_1 and ρ_2 corresponding input states $|\psi_1\rangle$ and $|\psi_2\rangle$ are shown in Fig. 4(a,b), demonstrating state fidelities of $F_1 = 97.9 \pm 0.5\%$ and $F_2 = 96.1 \pm 0.5\%$, respectively. These values significantly exceed the classical fidelity bound of 48% (see Section 9 in the Supplementary Materials for details) by more than 96 standard deviations, thereby demonstrating the reliable storage of qudits with d=5. The storage dimensionality of our device is intrinsically scalable: it scales directly with the number of individually addressable memory channels. Expansion is straightforward by fabricating two-dimensional waveguide arrays and employing crossed AOD pairs for addressing.

DISCUSSION

In summary, we have developed an 11-channel integrated quantum memory based on laser-written waveguide arrays fabricated in a $^{151}\text{Eu}^{3+}$: Y_2SiO_5 crystal. Individual channel addressing is achieved via AODs and each channel is independently controlled with on-chip electrode arrays, with negligible cross-talks. This multichannel design introduces novel functionalities to integrated quantum memories: random access quantum storage and high-dimensional quantum storage. demonstrate random access quantum storage of multiple time-bin qubits with an average fidelity exceeding 99%, utilizing three neighboring channels. Additionally, we achieve quantum storage of five-dimensional states with a fidelity greater than 96%, employing five neighboring channels. Harnessing the three-dimensional fabrication prowess of femtosecond-laser micromachining, the channel count can be readily scaled into the hundreds.

The active independent control of each storage channel can also be realized through optical control pulses via the spin-wave storage process [34, 45], which can provide significantly longer storage times. A storage time of milliseconds can be achieved at zero magnetic field [17], which could support applications in multiplexed and high-dimensional quantum repeaters. Operating at strong magnetic fields could further extend the storage time to minutes or even hours [27], enabling applications as high-density, transportable quantum memories [46, 47].

METHODS

Multichannel addressing and encoding. The 11 memory channels are addressed using a write/read AODs and lenses with a focal length of 75 mm. As illustrated in Fig. 1(a), the AODs are positioned on the focal plane of the lenses, enabling precise horizontal beam deflection and coupling the beam into and out of each waveguide, which has a core diameter of 30 µm core diameter. The RF sources for controlling the AODs are generated by a common arbitrary waveform generator (AWG). The frequency of the RF signal is scanned from 65.75 MHz to 104.25 MHz in steps of 3.85 MHz, allowing the AOD to deflect the beams into the 11 memory channels. The write AOD and the read AOD have opposite frequency offsets for each memory channel. As a result, the frequency differences between different channels are compensated after passing through the read AOD, facilitating interference measurements across multiple channels. Since all channels share the same optical setup, the relative phase between channels is inherently stable, enabling path encoding.

Time-bin qubit analyzer. The time-bin qubit analyzer functions as an unbalanced Mach-Zehnder interferometer, projecting time-bin qubits onto superposition states for analysis. It is implemented using an independent AFC memory with a storage time of T=200 ns. matching the time-bin separation interval. When a single photon passes through the AFC memory, it either transmits directly with probability p_0 or is emitted after a 200 ns delay with probability p_1 , labeled as early bin and late bin, respectively. By controlling the AFC structure to achieve $p_0 = p_1$, the device effectively functions as a time-bin splitter. Additionally, the phase $\theta = 2\pi\delta_f T$ between the early and late bin can be controlled by shifting the AFC frequency detuning δ_f [37].

After submission of this work, we note that multichannel storage has been demonstrated in an array of bulk $\Pr^{3+}: Y_2SiO_5$ crystals [48], though without random-access capability and high-dimensional storage.

ACKNOWLEDGEMENTS

This work is supported by the Innovation Program for Quantum Science and Technology (No. 2021ZD0301200, No.2024ZD0301400), the National Natural Science Foundation of China (Nos. 12222411, 11821404, and 12404572), the China Postdoctoral Science Foundation (2023M743400), and this work was partially carried out at the USTC Center for Micro and Nanoscale Research and Fabrication. Z.-Q.Z. acknowledges the support from the Youth Innovation Promotion Association CAS.

Z.-Q.Z. designed the experiment and supervised all aspects of this work; Z.-W.O. fabricated the device; Z.-W.O. and T.-X.Z. performed the experiment and analyzed the data; P.-J.L grew the crystal; X.-M.H. calculated the quantum channel capacity; Z.-W.O., T.-X.Z., X.-M.H and Z.-Q.Z. wrote the manuscript; Z.-Q.Z. and C.-F.L. supervised the project. All authors discussed the experimental procedures and results.

- * These authors contributed equally to this work.
- † zq_zhou@ustc.edu.cn
- [1] H. J. Kimble, Nature **453**, 1023 (2008).
- [2] A. I. Lvovsky, B. C. Sanders, and W. Tittel, Nature photonics 3, 706 (2009).
- [3] N. Sangouard, C. Simon, H. De Riedmatten, and N. Gisin, Reviews of Modern Physics 83, 33 (2011).
- [4] T.-S. Yang, Z.-Q. Zhou, Y.-L. Hua, X. Liu, Z.-F. Li, P.-Y. Li, Y. Ma, C. Liu, P.-J. Liang, X. Li, et al., Nature communications 9, 3407 (2018).
- [5] P. Kok, W. Munro, K. Nemoto, T. Ralph, J. P. Dowling, and G. Milburn, Reviews of Modern Physics 79, 797 (2007).
- [6] M. Hosseini, B. M. Sparkes, G. Hétet, J. J. Longdell, P. K. Lam, and B. C. Buchler, Nature 461, 241 (2009).
- [7] C. Vo, S. Riedl, S. Baur, G. Rempe, and S. Dürr, Physical Review Letters 109, 263602 (2012).
- [8] J. Nunn, N. Langford, W. Kolthammer, T. Champion, M. Sprague, P. Michelberger, X.-M. Jin, D. England, and I. Walmsley, Physical review letters 110, 133601 (2013).
- [9] G. Campbell, O. Pinel, M. Hosseini, T. C. Ralph, B. Buchler, and P. K. Lam, Physical review letters 113, 063601 (2014).
- [10] P. C. Humphreys, W. S. Kolthammer, J. Nunn, M. Barbieri, A. Datta, and I. A. Walmsley, Physical review letters 113, 130502 (2014).
- [11] X. Liu, X.-M. Hu, T.-X. Zhu, C. Zhang, Y.-X. Xiao, J.-L. Miao, Z.-W. Ou, P.-Y. Li, B.-H. Liu, Z.-Q. Zhou, et al., Nature Communications 15, 8529 (2024).
- [12] E. Saglamyurek, N. Sinclair, J. Jin, J. A. Slater, D. Oblak, F. Bussieres, M. George, R. Ricken, W. Sohler, and W. Tittel, Nature 469, 512 (2011).
- [13] T. Zhong, J. M. Kindem, J. G. Bartholomew, J. Rochman, I. Craiciu, E. Miyazono, M. Bettinelli, E. Cavalli, V. Verma, S. W. Nam, et al., Science 357, 1392 (2017).
- [14] Z.-Q. Zhou, C. Liu, C.-F. Li, G.-C. Guo, D. Oblak,

- M. Lei, A. Faraon, M. Mazzera, and H. de Riedmatten, Laser & Photonics Reviews 17, 2300257 (2023).
- [15] A. Seri, D. Lago-Rivera, A. Lenhard, G. Corrielli, R. Osellame, M. Mazzera, and H. de Riedmatten, Physical review letters 123, 080502 (2019).
- [16] R.-R. Meng, P.-X. Liu, X. Liu, T.-X. Zhu, P.-J. Liang, C. Zhang, Z.-Y. Tang, H.-Z. Zhang, J.-M. Cui, M. Jin, Z.-Q. Zhou, C.-F. Li, and G.-C. Guo, Efficient integrated quantum memory for light, Submitted.
- [17] Y.-P. Liu, Z.-W. Ou, T.-X. Zhu, M.-X. Su, C. Liu, Y.-J. Han, Z.-Q. Zhou, C.-F. Li, and G.-C. Guo, Science Advances 11, eadu5264 (2025).
- [18] N. Sinclair, E. Saglamyurek, H. Mallahzadeh, J. A. Slater, M. George, R. Ricken, M. P. Hedges, D. Oblak, C. Simon, W. Sohler, et al., Physical review letters 113, 053603 (2014).
- [19] S. Ecker, F. Bouchard, L. Bulla, F. Brandt, O. Kohout, F. Steinlechner, R. Fickler, M. Malik, Y. Guryanova, R. Ursin, et al., Physical Review X 9, 041042 (2019).
- [20] M. Erhard, M. Krenn, and A. Zeilinger, Nature Reviews Physics 2, 365 (2020).
- [21] Y. Zheng, H. Sharma, and J. Borregaard, PRX Quantum 3, 040319 (2022).
- [22] E. T. Campbell, Physical review letters 113, 230501 (2014).
- [23] B. P. Lanyon, M. Barbieri, M. P. Almeida, T. Jennewein, T. C. Ralph, K. J. Resch, G. J. Pryde, J. L. O'brien, A. Gilchrist, and A. G. White, Nature Physics 5, 134 (2009).
- [24] N. Jiang, Y.-F. Pu, W. Chang, C. Li, S. Zhang, and L.-M. Duan, npj Quantum Information 5, 28 (2019).
- [25] S. Langenfeld, O. Morin, M. Körber, and G. Rempe, npj Quantum Information 6, 86 (2020).
- [26] S. Zhang, J. Shi, Z. Cui, Y. Wang, Y. Wu, L. Duan, and Y. Pu. Physical Review X 14, 021018 (2024).
- [27] Y. Ma, Y.-Z. Ma, Z.-Q. Zhou, C.-F. Li, and G.-C. Guo, Nature communications 12, 2381 (2021).
- [28] T.-X. Zhu, C. Liu, M. Jin, M.-X. Su, Y.-P. Liu, W.-J. Li, Y. Ye, Z.-Q. Zhou, C.-F. Li, and G.-C. Guo, Physical Review Letters 128, 180501 (2022).
- [29] S. P. Horvath, M. K. Alqedra, A. Kinos, A. Walther, J. M. Dahlström, S. Kröll, and L. Rippe, Physical Review Research 3, 023099 (2021).
- [30] C. Liu, T.-X. Zhu, M.-X. Su, Y.-Z. Ma, Z.-Q. Zhou, C.-F. Li, and G.-C. Guo, Physical Review Letters 125, 260504 (2020).
- [31] H. De Riedmatten, M. Afzelius, M. U. Staudt, C. Simon, and N. Gisin, Nature 456, 773 (2008).
- [32] M. Afzelius, C. Simon, H. De Riedmatten, and N. Gisin, Physical Review A—Atomic, Molecular, and Optical Physics 79, 052329 (2009).
- [33] J.-S. Tang, Z.-Q. Zhou, Y.-T. Wang, Y.-L. Li, X. Liu, Y.-L. Hua, Y. Zou, S. Wang, D.-Y. He, G. Chen, et al., Nature communications 6, 8652 (2015).
- [34] A. Ortu, A. Holzäpfel, J. Etesse, and M. Afzelius, npj Quantum Information 8, 29 (2022).
- [35] X. Liu, J. Hu, Z.-F. Li, X. Li, P.-Y. Li, P.-J. Liang, Z.-Q. Zhou, C.-F. Li, and G.-C. Guo, Nature 594, 41 (2021).
- [36] O. Collins, S. Jenkins, A. Kuzmich, and T. Kennedy, Physical review letters 98, 060502 (2007).
- [37] K. Kutluer, E. Distante, B. Casabone, S. Duranti, M. Mazzera, and H. de Riedmatten, Physical Review Letters 123, 030501 (2019).
- [38] M. Gündoğan, P. M. Ledingham, K. Kutluer,

- M. Mazzera, and H. De Riedmatten, Physical review letters **114**, 230501 (2015).
- [39] D.-C. Liu, P.-Y. Li, T.-X. Zhu, L. Zheng, J.-Y. Huang, Z.-Q. Zhou, C.-F. Li, and G.-C. Guo, Physical Review Letters 129, 210501 (2022).
- [40] H. Bechmann-Pasquinucci and A. Peres, Physical Review Letters 85, 3313 (2000).
- [41] N. J. Cerf, M. Bourennane, A. Karlsson, and N. Gisin, Physical review letters 88, 127902 (2002).
- [42] S.-Y. Lan, A. Radnaev, O. Collins, D. Matsukevich, T. Kennedy, and A. Kuzmich, Optics express 17, 13639 (2009).
- [43] Y. Pu, N. Jiang, W. Chang, H. Yang, C. Li, and L. Duan, Nature communications 8, 15359 (2017).
- [44] J. L. O'Brien, G. J. Pryde, A. Gilchrist, D. F. James, N. K. Langford, T. C. Ralph, and A. G. White, Physical review letters 93, 080502 (2004).
- [45] Y.-Z. Ma, M. Jin, D.-L. Chen, Z.-Q. Zhou, C.-F. Li, and G.-C. Guo, Nature Communications 12, 4378 (2021).
- [46] M. Gündoğan, J. S. Sidhu, M. Krutzik, and D. K. Oi, Optica Quantum 2, 140 (2024).
- [47] J. Bland-Hawthorn, M. J. Sellars, and J. G. Bartholomew, JOSA B 38, A86 (2021).
- [48] M. Teller, S. Plascencia, S. Grandi, and H. de Riedmatten, Phys. Rev. X 15, 031053 (2025).
- [49] P. Jobez, N. Timoney, C. Laplane, J. Etesse, A. Ferrier, P. Goldner, N. Gisin, and M. Afzelius, Physical Review A 93, 032327 (2016).
- [50] R. M. Macfarlane, A. Arcangeli, A. Ferrier, and P. Goldner, Physical Review Letters 113, 157603 (2014).
- [51] D. F. James, P. G. Kwiat, W. J. Munro, and A. G. White, Physical Review A 64, 052312 (2001).
- [52] A. S. Holevo, IEEE Transactions on Information Theory 44, 269 (2002).
- [53] B. Schumacher and M. D. Westmoreland, Physical Review A 56, 131 (1997).
- [54] S. Lloyd, Physical Review A 55, 1613 (1997).
- [55] P. W. Shor, in lecture notes, MSRI Workshop on Quantum Computation, Vol. 5 (2002).
- [56] I. Devetak, IEEE Transactions on Information Theory 51, 44 (2005).
- [57] B. Schumacher and M. A. Nielsen, Physical Review A 54, 2629 (1996).
- [58] M.-X. Dong, W.-H. Zhang, L. Zeng, Y.-H. Ye, D.-C. Li, G.-C. Guo, D.-S. Ding, and B.-S. Shi, Physical Review Letters 131, 240801 (2023).

Supplementary Materials for "Multichannel and high dimensional integrated photonic quantum memory"

Zhong-Wen Ou $^{1,2,3,*},$ Tian-Xiang Zhu 1,2,3,* Peng-Jun Liang 1,2,3,4 Xiao-Min Hu 1,2,3,4 Zong-Quan Zhou 1,2,3,4,† Chuan-Feng Li 1,2,3,4 and Guang-Can Guo 1,2,3,4

Laboratory of Quantum Information, University of Science and Technology of China, Hefei 230026, China
 Anhui Province Key Laboratory of Quantum Network, University of Science and Technology of China, Hefei 230026, China
 CAS Center For Excellence in Quantum Information and Quantum Physics, University of Science and Technology of China, Hefei 230026, China

 $^{^4}$ Hefei National Laboratory, University of Science and Technology of China, Hefei 230026, China

1. Details of the memory device

The device architecture is illustrated in Fig. S1(a). Waveguide arrays are sculpted with a femtosecond-laser micromachining (FLM) platform (WOPhotonics, Lithuania). The laser parameters include a wavelength of 1030 nm, a repetition rate of 201.9 kHz, a pulse duration of 219 fs, and a pulse energy of 80 nJ. The beam, polarized along the crystal's D2-axis, is focused 25 μ m below the crystal surface through a $100\times$, NA=0.7 objective and translated along the b-axis at a speed of 5 mm/s. Each depressed cladding waveguide consists of 32 parallel tracks arranged in a 30- μ m radius circle. For signal mode with polarization along the D1 axis, we measure an optimized insertion loss of 0.46 dB (a device transmission of 90%), which includes propagation, coupling, and Fresnel losses. The guided mode is nearly Gaussian, with fitted full width at half maximum (FWHM) of $14.6\times15.1~\mu$ m (Fig. S1(b)). Eleven waveguides are fabricated in the crystal with a spacing of 250 μ m. The absorption of 151 Eu³⁺ ion inside the optical waveguide is measured as $\alpha = 4.3$ /cm with a broadening of 1.46 GHz, closely matching bulk values ($\alpha = 4.6$ /cm, 1.41 GHz).

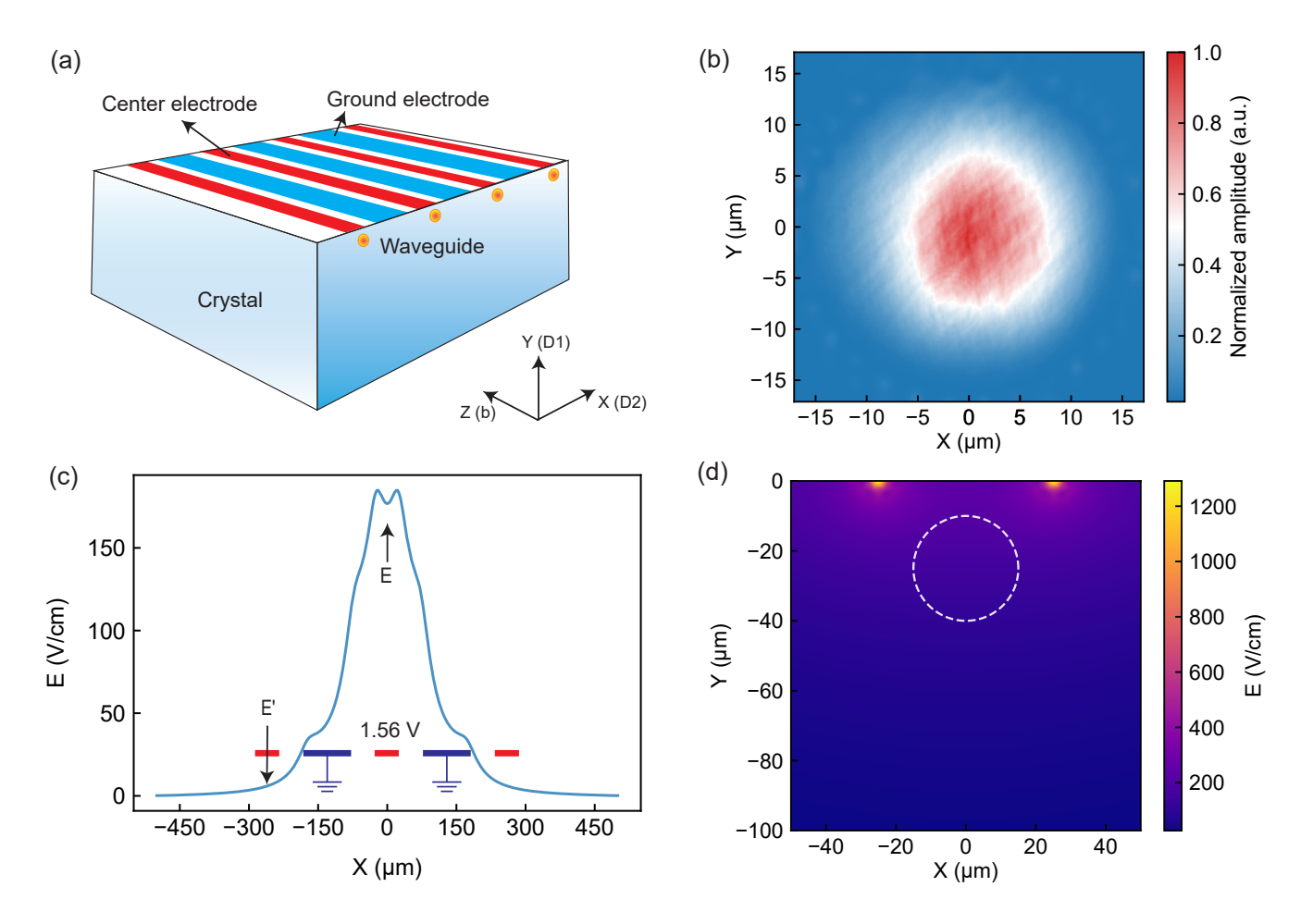


Fig. S1. Multichannel memory device. (a) Schematic diagram of the memory structure. A waveguide array is aligned along the crystal's b axis with an inter-waveguide spacing of 250 μ m. The central electrode is positioned directly above the waveguide, with its center offset by 25 μ m from the waveguide center. (b) Normalized mode field distribution at waveguide end-facet. (c) Electric field distribution along the X-axis at 25 μ m depth below the electrode. The central electrode biased is 1.56 V, where E denotes the electric field magnitude beneath the central electrode, and E' represents the residual field intensity beneath the adjacent electrode. (d) Electric field distribution in the XY cross-section; the dashed circle indicates the optical waveguide location.

After waveguide inscription, electrode arrays are patterned on the crystal surface via lift-off lithography. Each central electrode, with a width of 50 μ m, is aligned directly above a waveguide and flanked by 100- μ m wide ground electrodes set 125 μ m away, a geometry chosen to suppress inter-electrode crosstalk. A bias of 1.56 V applied to the central electrode produces the simulated field maps shown in Figs. S1(c,d). The electric field is E=176.8 V/cm at the waveguide center with a residual crosstalk field E'=7.0 V/cm $\approx 0.04E$, confirming a negligible electrical crosstalk

in agreement with the measurements in Fig. S5.

2. Details of experiment setup

As shown in Fig. S2(a), the memory device is cooled to approximately 3.2 K in a closed-cycle cryostat (Montana Instruments). The 580 nm laser (Precilasers) is generated by sum-frequency of a 1537 nm laser and a 932.5 nm laser. The laser linewidth after external locking is approximately 0.17 kHz. The signal and pump beams are modulated using double-pass acousto-optic modulators (AOMs) driven by an arbitrary waveform generator (AWG, Zurich Instruments). This AWG also controls the Write/Read AODs (Brimrose) and electrode arrays.

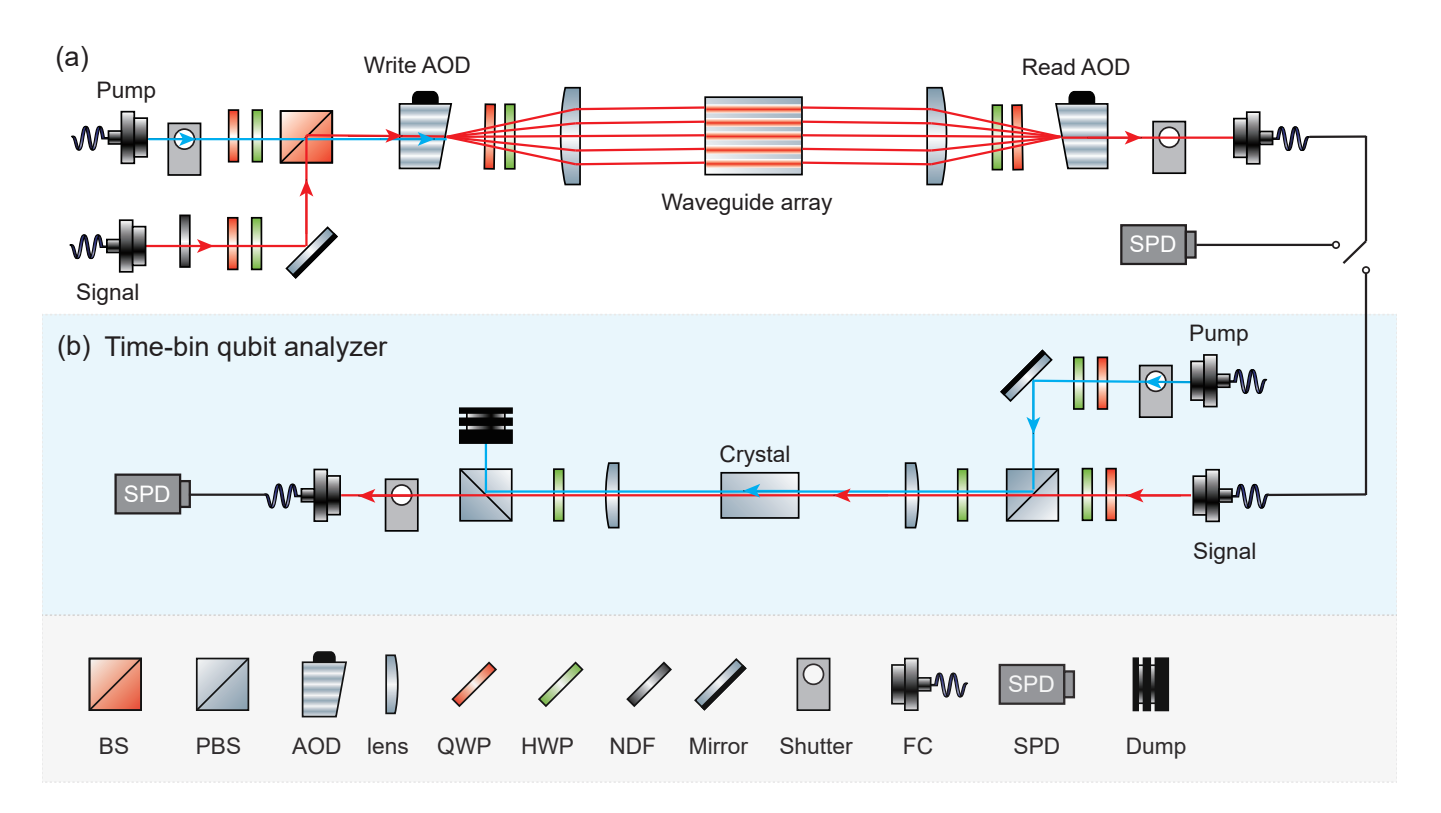


Fig. S2. Detailed experimental optical setup. The optical configuration comprises two subsystems: multichannel storage unit (a) and time-bin qubit analyzer unit (b). (a), The signal beam is attenuated to single-photon level via a neutral density filters (NDF) and combined with pump beam through a 90:10 (R:T) beam splitter (BS). The polarization control is achieved using a half-wave plate (HWP) and a quarter-wave plate (QWP). The combined beam is addressed to 11 memory channels (only 5 channels are schematically shown) through a write acoustic optical deflector (AOD) and a lens with 75 mm focal length. Subsequent readout paths follow similar configurations, directing the output to either a single-photon detector (SPD) or a time-bin qubit analyzer. (b), The signal and pump beams are combined via a polarizing beam splitter (PBS), with polarization controlled by a HWP and a QWP. A 4f imaging system focuses the beam into the ¹⁵¹Eu³⁺:Y₂SiO₅ crystal. The readout signal and the transmitted pump beams are separated by the PBS. Optical shutters are implemented throughout the system to protect SPD. Fiber collimator (FC).

The time-bin qubit analyzer shown in Fig. S2(b) characterizes the fidelity of stored time-bin qubits. The pump beam initializes and prepares the AFC structure with a comb spacing of 500 kHz in the $^{151}\text{Eu}^{3+}$:Y₂SiO₅ crystal. In this crystal, the signal input splits into two components: a transmitted portion and a 1^{st} -order AFC echo emits at T=200 ns. For time-bin qubit analyzer operation, the comb structure must be adjusted to maintain amplitude balance between the transmitted component and the AFC echo. Spectral shifting of the AFC enables control over their relative phase $\theta=2\pi\delta_f T$, thereby modifying the readout phase, where δ_f denotes the frequency detuning.

We present a detailed characterization of component efficiency within the storage unit, as illustrated in Fig. S3(a). The total optical path efficiency across different memory channels ranges from 16% to 52%. Optical path efficiency is relatively low for channels located on both sides. This reduction primarily results from two factors: losses due to AOD diffraction, and mode mismatch during waveguide coupling caused by spherical lens aberration. The total

transmission of the eleven waveguides ranges from 71% to 90%. Notably, the transmission of some waveguides exceeds the 84% transmittance of the uncoated crystal itself. This enhancement is attributed to the waveguide cavity effect since the crystal end face provides a reflectivity of approximately 8%.

The optical crosstalk between storage channels is defined as $C_{ij} = 10 \ln(n_{ij}/n_{ii})$, where n_{ij} represents the photon counts detected at the output of the j-th channel when photons are input into the i-th channel. Our measurements indicate that the optical crosstalk between storage channels remains below -40 dB. This excellent isolation results from the wide waveguide spacing as well as the effective photon confinement within the waveguide structure. Additionally, in Fig. S5(b) in Section 3, we present a quantitative measurement of electrical crosstalk of our device.

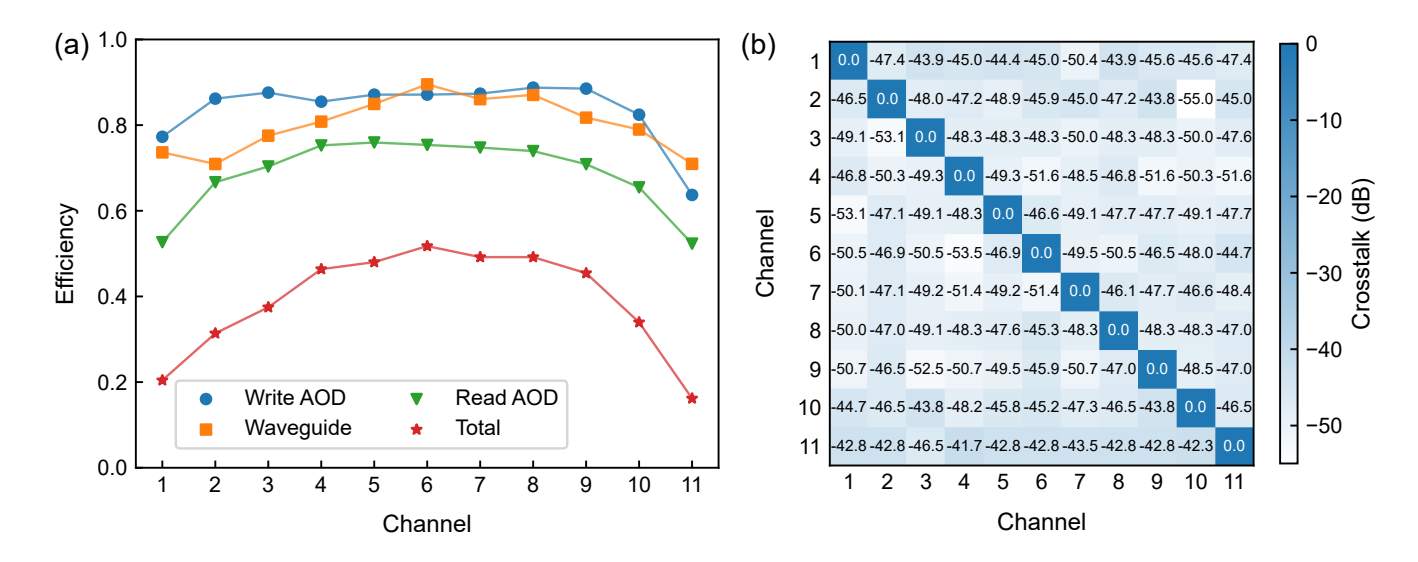


Fig. S3. (a) Components efficiency for individual storage channels. Total efficiency is defined as the ratio of the output after final single-mode collection to the input prior to injection into the write AOD. (b) Inter-channel crosstalk performance.

3. SMAFC storage protocol

The SMAFC protocol enables on-demand quantum storage by introducing an electric field to manipulate atomic coherence [28–30]. Due to the space-group symmetry of Y_2SiO_5 crystal, applying an electric field along the crystal's D1 axis results in two distinct classes of ions experiencing the same Stark frequency shifts of magnitude, but in opposite directions. The shift magnitude is given by $\Omega = (\mu_g - \mu_e) \cdot \mathbf{E}/h$, where μ_g and μ_e denote the electric dipole moments of the ground and excited states, respectively, \mathbf{E} is the applied electric field, and h is Planck's constant. After the photon absorption at t = 0, applying an electrical pulse with duration $T = 1/(4\Omega)$ during the time interval $[0, 1/\Delta]$ effectively suppresses the emission of the standard AFC echo. Subsequently, a second pulse of negative polarity applied during the time interval $[(n-1)/\Delta, n/\Delta]$ induces photon re-emission at $t = n/\Delta$, generating the n^{th} -order SMAFC echo. The storage efficiency of SMAFC is given by

$$\eta = \tilde{d}^2 e^{-\tilde{d}} e^{-t^2 \tilde{\gamma}^2},\tag{S1}$$

where $\tilde{\gamma}$ is related to the comb FWHM by $\tilde{\gamma}=2\pi\gamma/\sqrt{8\ln 2},\ \tilde{d}$ is the effective absorption depth of the comb defined as $\tilde{d}=\frac{d}{F}\sqrt{\frac{\pi}{4\ln 2}},\ F$ is the the comb finesse, and d is the peak absorption of the combs [29].

The energy level structure of the $^7F_0\to ^5D_0$ transition of $^{151}\mathrm{Eu}^{3+}$ ions is illustrated in Fig. S4(a) and the

The energy level structure of the ${}^{7}F_{0} \rightarrow {}^{5}D_{0}$ transition of ${}^{151}\text{Eu}^{3+}$ ions is illustrated in Fig. S4(a) and the time sequence for SMAFC storage is illustrated in Fig. S4(c). During initialization, we optically pump ions within frequency ranges $[f_{0}+10.15 \text{ MHz}, f_{0}+90.85\text{MHz}]$ and $[f_{0}-90.85\text{MHz}, f_{0}-10.15\text{MHz}]$ to enhance the optical depth and bandwidth, creating an absorption profile centered at f_{0} with 20 MHz bandwidth and with an absorption depth of ~ 10.7 [11, 28]. Subsequently, a parallel comb preparation scheme [49] is used to generate an AFC with a comb tooth spacing of $\Delta = 2$ MHz or 200 kHz. After the input photons are absorbed by the AFC structure, we apply an electric pulse with a duration of 50 ns and a voltage of 1.56 V in the time interval $[0, 1/\Delta]$, and a negative polarity pulse in the time interval $[(n-1)/\Delta, n/\Delta]$ to the electrodes, enabling the retrieval of the n^{th} -order echo at $t = n/\Delta$.

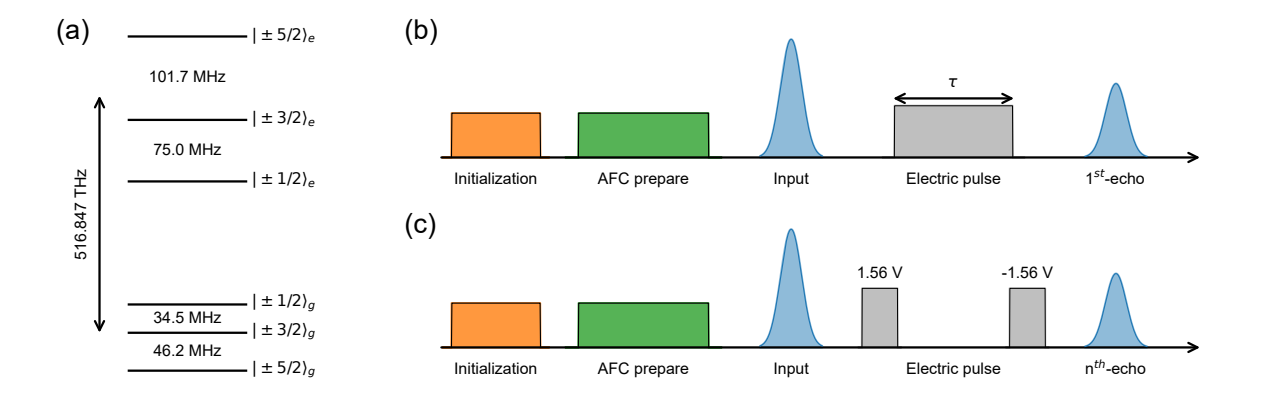


Fig. S4. (a) Level structure for site-1 151 Eu $^{3+}$ ions at zero magnetic field. (a) Time sequence for Stark modulation measurements with variable modulation pulse duration τ . (c) Time sequence for SMAFC storage protocol.

Before SMAFC storage implementation, we characterize the Stark modulation induced intereference of $^{151}\mathrm{Eu^{3+}}$ ions using the sequence presented in Fig. S4(b). The amplitude of the 1^{st} -order echo is measured while varying electric pulse duration τ (Fig. S5(a)). The echo amplitude exhibits damped oscillations with increasing τ . For a uniform electric field, echo intensity follows: $I_{\rm echo} \propto \cos^2(2\pi\Omega\tau)$. Accounting for electric field inhomogeneity across the ensemble, the echo intensity becomes: $I_{\rm echo} \propto \mathrm{e}^{-\tau^2/\tau_{\rm inh}^2}\cos^2(2\pi\Omega\tau)$, where $\tau_{\rm inh}$ characterizes the electric field inhomogeneity induced decoherence timescale. Experimental data show excellent agreement with theoretical fits (Fig. S5(a)), yielding: $\Omega = 12.7$ MHz, $\tau_{\rm inh} = 70.1$ ns. The Stark coefficient is derived as: $\mu = 28.0$ kHz/(V· cm⁻¹). This result is consistent with previously reported values [30, 50].

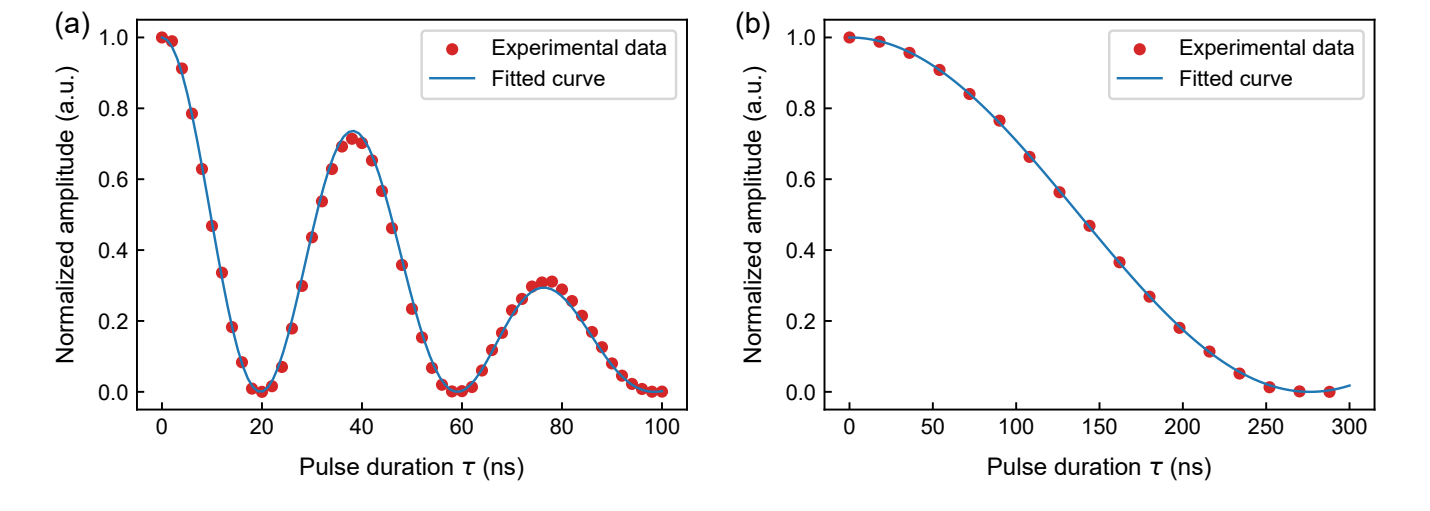


Fig. S5. (a) Normalized amplitude of the 1^{st} -order AFC echo as a function of modulation pulse duration τ , measured under 4 V electrical pulses. (b) Normalized amplitude of the 1^{st} -order AFC echo versus modulation pulse duration τ , measured under 5 V pulses applied to the electrode adjacent to the central electrode. For both (a) and (b), red markers denote experimental data; blue solid lines represent theoretical fitted curves.

In order to further evaluate the impact of electrical crosstalk on the storage efficiency, an electric field is applied to the adjacent center electrode to perform the similar measurements on Stark modulation. The measured 1^{st} -order AFC echo under this configuration is shown in Fig. S5(b). Data fitting yields $\Omega' = 0.9$ MHz, corresponding to a residual electric field E' = 0.05E (E denotes the electric field of the central electrode), which is consistent with the electric field simulation results presented in Section 1. As a result, for the actual storage experiments (electric pulse duration of 50 ns with a voltage of 1.56 V), the efficiency attenuation due to crosstalk is estimated to be below 1%.

We prepare AFC with $\Delta=2$ MHz and $\Delta=200$ kHz, corresponding to SMAFC storage with step of $1/\Delta=0.5$ μs and $1/\Delta=5$ μs , respectively. For $\Delta=2$ MHz, the preparation time of AFC is 2 s. Fig. S6(a) displays the photon

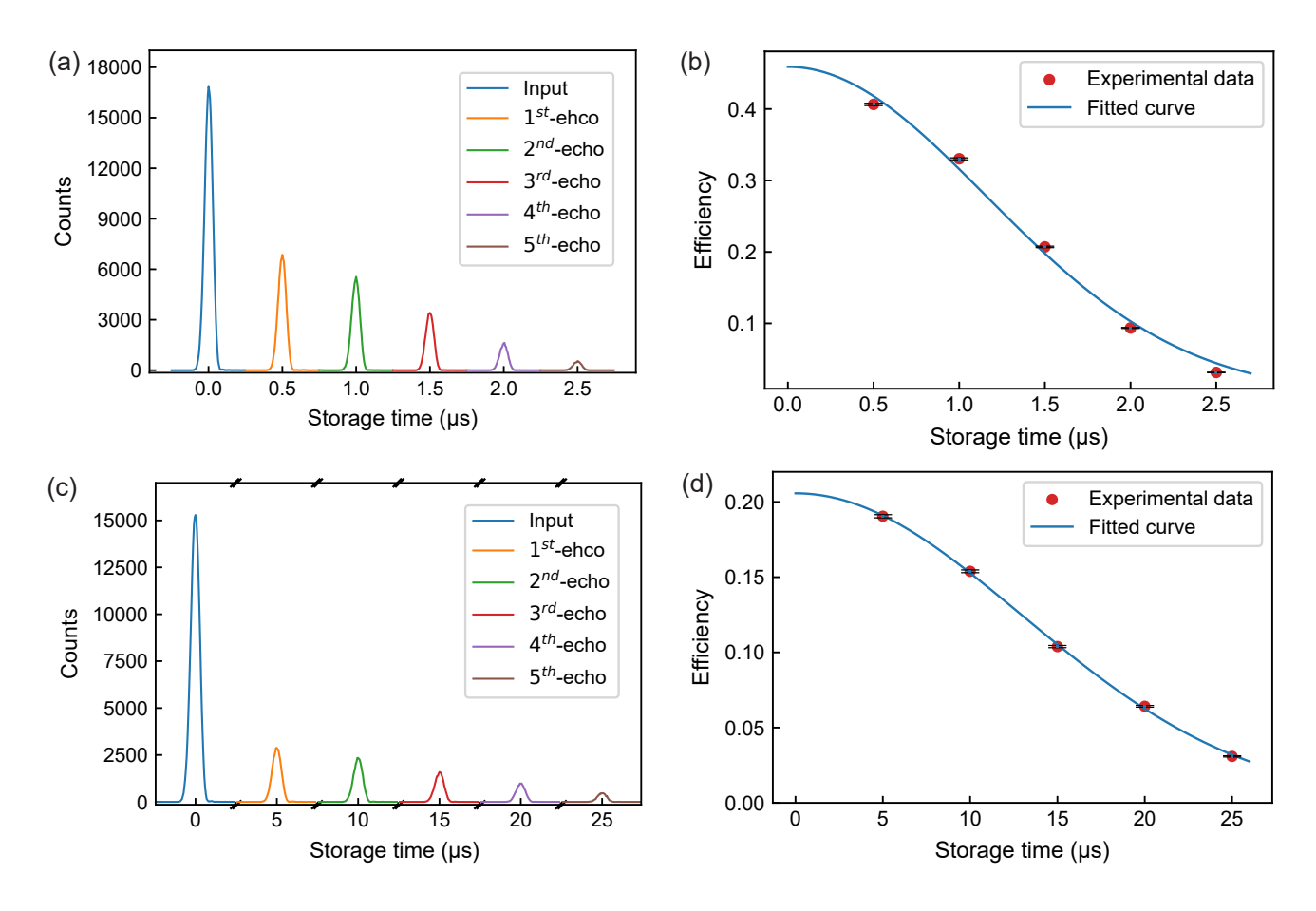


Fig. S6. Photon counting histogram for SMAFC storage with $1/\Delta = 0.5$ µs (a) and $1/\Delta = 5$ µs (c). The SMAFC storage efficiency as a function of storage time for $1/\Delta = 0.5$ µs (b) and $1/\Delta = 5$ µs (d). For (b) and (d), red dots denote experimental data, and blue solid lines represent theoretical fitted curves.

counting histogram for SMAFC storage with a maximum storage time of 2.5 μ s. Fig. S6(b) shows time-dependent storage efficiency. Fitting the data with Eq. S1 yields the AFC finesse F=8.7 and the absorption depth of the comb peaks d=10.6. For $\Delta=200$ kHz, the preparation time of AFC is 5 s. Fig. S6(c) displays the photon counting histogram for SMAFC storage with a maximum storage time of 25 μ s. Fig. S6(d) shows time-dependent storage efficiency with fitted F=9.8 and d=5.7. To comprehensively characterize the storage performance across all 11 channels, we implement SMAFC storage for each memory channel with $\Delta=2$ MHz. Storage efficiency versus time for all channels are shown in Fig. S7. All channels exhibit nearly identical efficiency, demonstrating high uniformity across 11 memory channels.

4. Random access quantum memory

This section provide the details about random access quantum storage of multiple time-bin qubits. Time-bin qubits are prepared with a double-pass AOM. They are mapped into memory channels using the write AOD. Subsequently, the stored time-bin qubits can be read out in arbitrary order using a read AOD and a precisely controlled electrical pulse sequence. In addition to the data presented in the main text, here we provide another example with readout order of 1-2-3 in Fig. S8. In Fig. S8(a), qubits $Q_1:|e\rangle/|l\rangle$, $Q_2:|e\rangle/|l\rangle$, and $Q_3:|e\rangle/|l\rangle$ are sequentially written into the memory channels and retrieved in the order 1-2-3. The storage fidelity for the states $|e\rangle$ and $|l\rangle$ is defined as $F_{|e\rangle(|l\rangle)} = \frac{S+N}{S+2N}$, where N represents the noise counts and S the signal counts. When Q_1 , Q_2 , and Q_3 are encoded in superposition states $(|e\rangle+i|l\rangle)/\sqrt{2}$ and $(|e\rangle+e^{i3\pi/4}|l\rangle)/\sqrt{2}$, the readout state is measured using the time-bin analyzer. The readout basis is defined as $(|e\rangle+e^{i\theta}|l\rangle)/\sqrt{2}$, where θ denotes the read-out phase. The resulting interference are shown in Fig. S8(b,c). The fidelity for superposition states is defined as F = (V+1)/2, where V denotes the measured

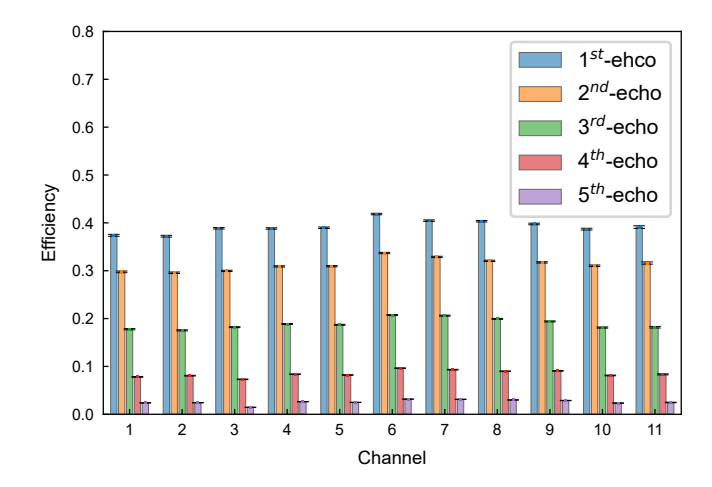


Fig. S7. SMAFC storage efficiency across 11 memory channels with $\Delta=2$ MHz.

interference visibility.

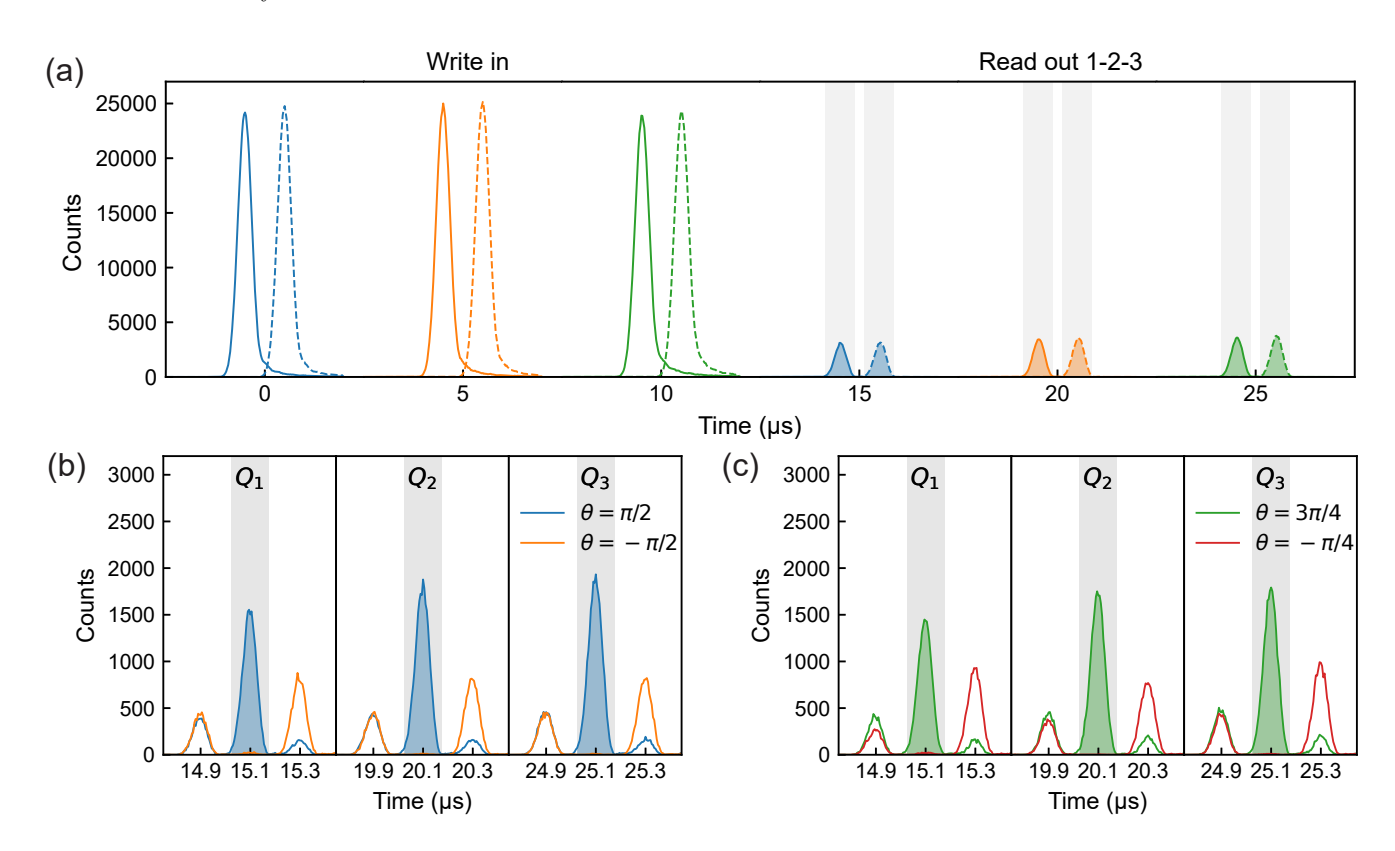


Fig. S8. Random access quantum storage of time-bin qubits with read-out in the order 1-2-3. (a) Photon counting histogram for time-bin qubit storage. $Q_1:|e\rangle/|l\rangle$ (blue solid / dashed), $Q_2:|e\rangle/|l\rangle$ (orange solid / dashed) and $Q_3:|e\rangle$ (green solid / dashed) are written and read-out in the order 1-2-3. (b) Interference histogram for qubits Q_1, Q_2, Q_3 prepared in $(|e\rangle+i|l\rangle)/\sqrt{2}$. The read-out phases are set to $\theta=\pi/2$ (blue solid) and $\theta=-\pi/2$ (orange solid). Measured visibilities for the qubits are 97.3 \pm 0.1%, 98.9 \pm 0.1%, and 99.1 \pm 0.1%, respectively. (c) Interference histogram for qubits Q_1, Q_2, Q_3 prepared in $(|e\rangle+e^{i3\pi/4}|l\rangle)/\sqrt{2}$. The read-out phases are set to $\theta=3\pi/4$ (green solid) and $\theta=-\pi/4$ (red solid). Measured visibilities for the qubits are 97.0 \pm 0.1%, 99.6 \pm 0.1%, and 98.8 \pm 0.1%, respectively.

Table SI presents the complete fidelity data for storing the states $|e\rangle$, $|l\rangle$, $(|e\rangle+i|l\rangle)/\sqrt{2}$, and $(|e\rangle+e^{i3\pi/4}|l\rangle)/\sqrt{2}$, with read out orders 1-2-3, 2-1-3, and 3-2-1. The total fidelity is defined as $F_T = \frac{1}{3}F_{el} + \frac{2}{3}F_{\pm}$, where $F_{el} = (F_{|e\rangle} + F_{|l\rangle})/2$

Order		$F_{ e\rangle}$	$F_{ l\rangle}$	$F_{(e\rangle+i l\rangle)/\sqrt{2}}$	$F_{(e\rangle+e^{i3\pi/4} l\rangle)/\sqrt{2}}$	F_T
	Q_1	$99.8 \pm 0.1\%$	$99.9 \pm 0.1\%$	$98.6 \pm 0.1\%$	$98.5 \pm 0.1\%$	$99.0 \pm 0.1\%$
1-2-3	Q_2	$99.9 \pm 0.1\%$	$99.9 \pm 0.1\%$	$99.5 \pm 0.1\%$	$99.8 \pm 0.1\%$	$99.7 \pm 0.1\%$
	Q_3	$99.8 \pm 0.1\%$	$99.9 \pm 0.1\%$	$99.6 \pm 0.1\%$	$99.4 \pm 0.1\%$	$99.6 \pm 0.1\%$
	Q_1	$99.8 \pm 0.1\%$	$99.9 \pm 0.1\%$	$99.1 \pm 0.1\%$	$99.0 \pm 0.1\%$	$99.3 \pm 0.1\%$
2-1-3	Q_2	$99.8 \pm 0.1\%$	$99.9 \pm 0.1\%$	$98.6 \pm 0.1\%$	$99.0 \pm 0.1\%$	$99.1 \pm 0.1\%$
	Q_3	$99.8 \pm 0.1\%$	$99.9 \pm 0.1\%$	$99.6 \pm 0.1\%$	$99.5 \pm 0.1\%$	$99.7 \pm 0.1\%$
	Q_1	$99.8 \pm 0.1\%$	$99.9 \pm 0.1\%$	$99.3 \pm 0.1\%$	$99.0 \pm 0.1\%$	$99.4 \pm 0.1\%$
3-2-1	Q_2	$99.8 \pm 0.1\%$	$99.9 \pm 0.1\%$	$99.8 \pm 0.1\%$	$99.6 \pm 0.1\%$	$99.8 \pm 0.1\%$
	Q_3	$99.7 \pm 0.1\%$	$99.9 \pm 0.1\%$	$99.3 \pm 0.1\%$	$98.6 \pm 0.1\%$	$99.2 \pm 0.1\%$

Table. SI. The fidelities of the three time-bin qubits after being retrieved in different orders.

and $F_{\pm} = (F_{(|e\rangle+i|l\rangle)/\sqrt{2}} + F_{(|e\rangle+e^{i3\pi/4}|l\rangle)/\sqrt{2}})/2$. The total fidelity exceeds 99% for all readout sequences, which is far beyond the classical bound (81.8%, see details in Section 9), demonstrating the excellent performance of the random access quantum memory. Table SII lists storage efficiencies of time-bin qubits for different readout orders, ranging from 2.9% to 18.7%.

Table. SII. Storage efficiencies for time-bin qubits Q_1 , Q_2 , and Q_3 with readout orders 1-2-3, 2-1-3, and 3-2-1.

Order	η_{Q_1}	η_{Q_2}	η_{Q_3}
1-2-3	$10.2 \pm 0.1\%$	$11.3 \pm 0.1\%$	$11.9 \pm 0.1\%$
2 - 3 - 1	$6.1\pm0.1\%$	$15.2\pm0.1\%$	$11.6\pm0.1\%$
3-2-1	$18.7\pm0.1\%$	$10.5\pm0.1\%$	$2.9 \pm 0.1\%$

5. Quantum storage for path-encoded qubits

Path-encoded qubits are prepared and measured via AODs. We dedicate the channel pairs (n, m) = (4,5), (6,7) and (8,9) to store the path qubits: $|C_n\rangle$, $(|C_n\rangle + |C_m\rangle)/\sqrt{2}$ and $(|C_n\rangle + i|C_m\rangle)/\sqrt{2}$, setting the mean photon number to $\mu = 0.38$ per qubit. Fig. S9(a,b) present photon-counting histograms for $|C_4\rangle$ and $(|C_6\rangle + |C_7\rangle)/\sqrt{2}$, retrieved on demand after 0.5 μ s and 1.0 μ s, respectively. The corresponding reconstructed density matrices are shown in Fig. S9(c,d). We further quantify the storage infidelity across all memory channel pairs for variable storage times (Fig. S9(e)), demonstrating that all path qubits retain a fidelity exceeding 98%.

6. High-dimensional quantum state tomography

Here we employ high-dimensional quantum state tomography (QST) for reconstructing the density matrix ρ of qudit states [51]. For a d-dimensional quantum state, the density matrix ρ_d admits the decomposition

$$\rho_d = \frac{1}{d} \sum_{i=0}^{d^2 - 1} r_i \hat{\lambda}_i, \tag{S2}$$

where $\hat{\lambda}_0 = I_{d \times d}$ and $\hat{\lambda}_i$ ($0 < i \le d^2 - 1$) denote the generators of the SU(d) group. The coefficients r_i correspond to expectation values: $r_i = \langle \hat{\lambda}_i \rangle = \text{Tr}(\rho \hat{\lambda}_i)$. Given a complete set of measurement bases $\{\hat{\mu}_i = |\psi_i\rangle \langle \psi_i|\}$, the projection operators can be expressed in terms of $\hat{\lambda}_i$ as: $\hat{\mu}_i = \sum_j A_i^j \hat{\lambda}_j$. For a d-dimensional quantum system, projective measurements yield outcomes: $n_i = N \text{Tr}(\rho_d \hat{\mu}) = N \sum_j A_i^j \text{Tr}(\rho \hat{\lambda}_i) = N \sum_j A_i^j r_j$ (N is a normalization constant determinable from experimental data). The density matrix can formally be reconstructed through linear inversion: $\rho = N^{-1} \sum_{i,j} (A_i^j)^{-1} n_i \hat{\lambda}_j / d$. However, direct inversion may violate the positive semi definiteness of the density matrix (e.g., $\text{Tr}(\rho) > 0$). To ensure physicality, we employ maximum likelihood estimation (MLE) – introducing positivity and trace constraints to obtain the optimal density matrix $\hat{\rho}$.

The density matrix ρ can be decomposed into the following form

$$\rho(t) = \hat{T}^{\dagger}(t)\hat{T}(t)/\text{Tr}\{\hat{T}^{\dagger}(t)\hat{T}(t)\},\tag{S3}$$

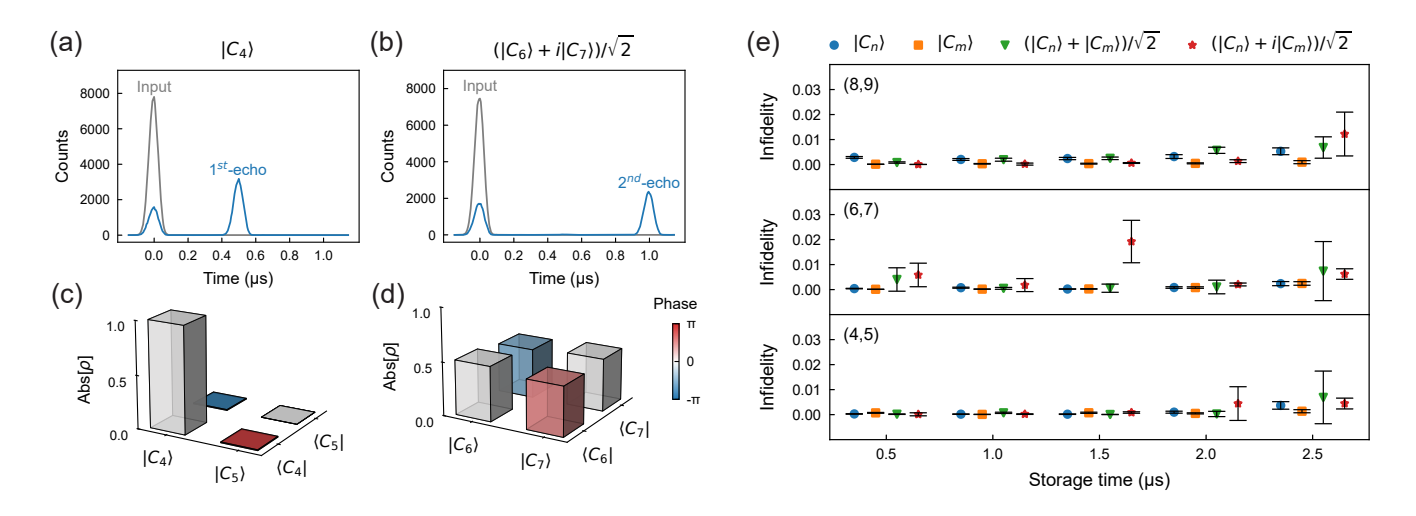


Fig. S9. On-demand quantum storage of path-encoded qubits. (a,c) Path qubit $|C_4\rangle$ stored for 0.5 μ s. Reconstructed density matrix achieves a fidelity of 99.9 \pm 0.1%. (b,d) Path qubit $(|C_6\rangle+i|C_7\rangle)/\sqrt{2}$ stored for 1.0 μ s. Reconstructed density matrix achieves a fidelity of 99.9 \pm 0.1%. (e) Measured storage infidelity for qubits encoded with memory channel pairs (4,5), (6,7) and (8,9), where infidelity is defined as 1-F. For (c) and (d), the height of the bar represents the absolute value of matrix elements, while the color denotes the phase.

where $\hat{T}(t)$ denotes a parameterized matrix, it is convenient to adopt an upper triangular representation. The parameter set $t = \{t_1, t_2, ..., t_{d^2}\}$ fully characterizes the matrix [51]. Crucially, this decomposition guarantees that ρ satisfies semi-positive definiteness. The density matrix can be reconstructed by numerically minimizing the function:

$$\mathcal{L}(t_1, t_2, ..., t_{d^2}) = \sum_{i=1}^{d^2} \frac{[N\langle \psi_i | \rho(t_1, t_2, ..., t_{d^2}) | \psi_i \rangle - n_i]^2}{2N\langle \psi_i | \rho(t_1, t_2, ..., t_{d^2}) | \psi_i \rangle},$$
(S4)

In our experimental configuration, the measurement bases are selected as: $\{|C_n\rangle, \{|C_n\rangle + |C_m\rangle/\sqrt{2}, (|C_n\rangle + i|C_m\rangle)/\sqrt{2}, 1 \le n < m \le d\}$. Photon counts for different projective measurements are recorded. The density matrix ρ_M is then reconstructed via MLE, with state fidelity computed as

$$F = \left(\text{Tr}\sqrt{\sqrt{\rho_M}\rho_i\sqrt{\rho_M}}\right)^2,\tag{S5}$$

where ρ_i is idea state.

7. Quantum process tomography

Quantum channels provide the natural framework for characterizing high-dimensional quantum storage processes. For a d-dimensional input state ρ , the storage operation is formally described by a completely positive trace-preserving (CPTP) map \mathcal{E} , such that the output state is given by $\mathcal{E}(\rho)$

$$\mathcal{E}(\rho) = \sum_{m,n=0}^{d^2} \chi_{mn} \hat{\lambda}_m \rho \hat{\lambda}_n^{\dagger}, \tag{S6}$$

where λ_m constitute the Kraus operator basis. For quantum memory characterization, we set $\lambda_0 = I_{d\times d}$ and let λ_i , $(0 < i \le d^2 - 1)$ denote the generators of SU(d) group. The process matrix χ with elements χ_{mn} provides a complete and unique description of the quantum channel \mathcal{E} . The process matrix χ is reconstructed via quantum process tomography (QPT) as follows: 1. Preparing an complete set of input states $\{\phi_i, 1 \le i \le d^2\}$. 2. Performing QST on the output states using the measurement basis $\{\psi_i, 1 \le i \le d^2\}$. 3. Reconstructing the matrix χ from the tomographic data. This protocol requires d^2 distinct input configurations and d^2 projective measurements per output state [44].

The tomographic data can be used to reconstruct the process matrix. The Hermitian matrix $\tilde{\chi}(t)$ is expressed in the form of Eq. S3 with parameters $t = \{t_1, t_2, ..., t_{d^2}\}$. This parameterization ensures that $\tilde{\chi}$ describes a trace-preservation process satisfying $\sum_{mn} \tilde{\chi}_{mn} \hat{\lambda}_m^{\dagger} \hat{\lambda}_n = I$. Using the maximum likelihood method (MLE), we can find the optimal estimate of the process matrix by minimizing the function:

$$f(t) = \sum_{i,j=1}^{d^2} \frac{1}{C} \left[c_{ij} - C \sum_{m,n=0}^{d^2 - 1} \langle \psi_j | \hat{\lambda}_m | \phi_i \rangle \langle \phi_i | \hat{\lambda}_n | \psi_j \rangle \tilde{\chi}_{mn}(t) \right]^2$$

$$+ \lambda \left[\sum_{m,n,k=0}^{d^2 - 1} \tilde{\chi}_{mn}(t) \operatorname{Tr}(\hat{\lambda}_n \hat{\lambda}_k \hat{\lambda}_m) - \delta_{k,0} \right],$$
(S7)

where c_{ab} denotes the photon counts for measurement basis $|\psi_b\rangle$ with input state $|\phi_a\rangle$, C is total count determined from the data, λ is a weighting factor and δ is the Kronecker delta. The parameter λ can be adjusted to ensure that the matrix is arbitrarily close to a completely positive map [44]. By minimizing the function f(t) through numerical optimization, we obtain the optimal process matrix χ and and quantum channel \mathcal{E} .

In our experimental configuration for four-dimensional quantum storage, the identical set of input states and measurement bases comprises: $\{|C_n\rangle, \ (|C_n\rangle + |C_m\rangle)/\sqrt{2}, \ (|C_n\rangle + i|C_m\rangle)/\sqrt{2}, \ 5 \le n < m \le 8\}$. This configuration requires 256 distinct measurement settings for photon counting. The reconstructed four-dimensional storage process matrix is presented in Fig. 3(c) of the main text, achieving a fidelity of $97.9 \pm 0.2\%$ to $\hat{\lambda}_0$.

8. Quantum channel capacity

The classical and quantum information transmission capabilities of a channel are characterized by its classical capacity C and quantum capacity Q, respectively. The classical capacity C of a channel represents the highest possible rate-measured in bits per use-at which classical information can be transmitted with vanishing error probability as the number of channel uses approaches infinity [52, 53]. A lower bound on the classical capacity can be established through the one-shot accessible information:

$$C_1 = \max_{\{P_x, P_x\}} \max_{\{P_y\}} H(X:Y), \tag{S8}$$

where the maximum is taken over all possible input ensembles p_x , ρ_x and output measurements P_y , and H(X:Y) denotes the mutual information between the random variables X and Y.

Defined as the asymptotic limit of infinitely many channel uses, the quantum capacity Q quantifies the maximum number of qubits that can be reliably transmitted per single use of the channel [54–56]. A lower bound on the quantum capacity is given by the one-shot coherent information:

$$Q_1 = \max_{\rho} I_c(\rho), \tag{S9}$$

where $T_c(\rho) := S[\mathcal{E}(\rho)] - S_e(\rho, \mathcal{E})$ is the coherent information of the state ρ [57], defined in terms of the von Neumann entropy, $S(\rho) := -\text{Tr}[\rho \log_2 \rho]$, and of the entropy exchange, $S_e(\rho, \mathcal{E}) := S[(\mathcal{T}_R \otimes \mathcal{E})(|\Psi_\rho\rangle\langle\Psi_\rho|)]$, with $|\Psi_\rho\rangle$ being any purification of ρ using a reference quantum system R.

To demonstrate the advantage of our system over conventional qubit-based memory in terms of storage capacity, we aim to determine the quantum channel capacity of the memory. Using process tomography, we obtained a high-dimensional process matrix capable of simulating arbitrary input and output states. By integrating optimization algorithms, we demonstrate that our 4-path storage scheme achieves a channel capacity of 1.932 ± 0.007 , surpassing the theoretical limit of qubit memory (which is 1).

At the same time, the exceptional performance of our quantum memory can be further validated through the entangled Schmidt number. We simulate the storage of a 4-dimensional maximally entangled state and, based on the reconstructed process matrix, calculate an output state fidelity of F = 0.975. This high fidelity not only surpasses the threshold for certifying a Schmidt number of 4 (F > 0.75) but also robustly demonstrates that our memory achieves a genuine 4-dimensional entanglement capability.

9. The conditional fidelity

To certify genuine quantum storage, we benchmark the process against the highest fidelity attainable with any classical measure-and-prepare strategy, accounting both for finite storage efficiency and the Poissonian statistics of the weak coherent input. For a system of N photonic qubits, the classical fidelity limit is $F = \frac{N+1}{N+2}$. For a general d-dimensional quantum system, the optimal state estimation fidelity is $F_d = \frac{N+1}{N+d}$. When high-dimensional quantum states are encoded via weak coherent states, it should be noted that photon numbers follow a Poisson distribution $P(\mu, N) = e^{-\mu} \mu^N / N!$ with mean photon number μ . The maximum achievable fidelity is given by

$$F_{\text{class}}^d(\mu) = \sum_{N>1} \frac{N+1}{N+d} \frac{P(\mu, N)}{1 - P(\mu, 0)},$$
 (S10)

This fidelity threshold holds for quantum memory with unit efficiency. If storage efficiency $\eta_M < 1$, the classical fidelity bound for d-dimensional systems is given by

$$F_{\text{class}}^{d}(\mu, \eta_{M}) = \frac{\frac{N_{\min} + 1}{N_{\min} + d} \gamma + \sum_{N \ge N_{\min} + 1} \frac{N + 1}{N + d} P(\mu, N)}{\gamma + \sum_{N > N_{\min} + 1} P(\mu, N)},$$
(S11)

where N_{\min} is the minimum i that satisfies $\sum_{N\geq i+1}P(\mu,N)\leq [1-P(\mu,0)]\eta_M$, and $\gamma=(1-P(\mu,0))\eta_M-\sum_{n\geq N_{\min}+1}P(\mu,n)$ [38, 58]. Fig. S10(a) plots the classical fidelity bound as a function of storage efficiency for mean photon numbers $\mu=0.38$ and $\mu=0.76$, corresponding to the inputs used for path and time-bin qubits, respectively. The experimentally measured fidelities (symbols) lie well above these bounds, confirming genuine quantum storage for both encodings. Fig. S10(b) shows the classical fidelity limit for dimensions d=2-5 at the measured efficiency $\eta_M=0.3$ (1 μ s high-dimensional storage). Our high-dimensional memories deliver fidelities that surpass the classical bound by substantial margins across all tested dimensions.

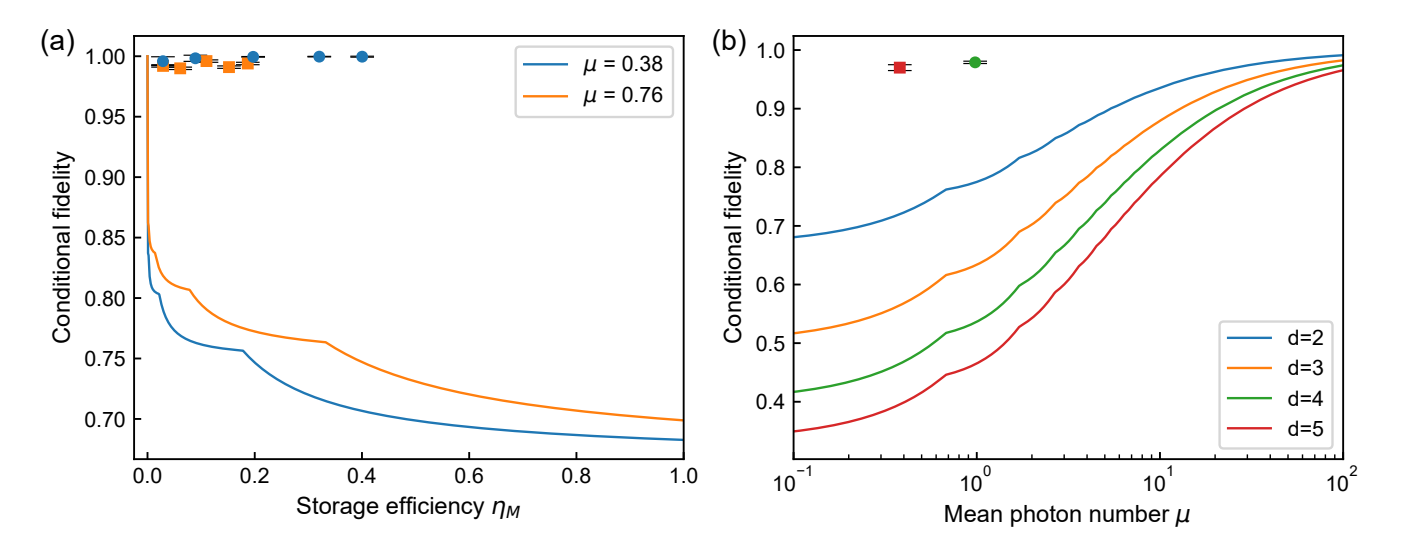


Fig. S10. (a) Maximum achievable fidelity for classical storage of a qubit, as a function of memory efficiency η_M at mean photon numbers $\mu=0.38$ (blue solid) and $\mu=0.76$ (orange solid). Experimental data: path qubits storage (blue circles) and time-bin qubits storage (orange squares). (b) Maximum achievable fidelity for classical storage of a qudit, as a function of mean photon number μ with a memory efficiency $\eta_M=0.3$. Experimental data: 4-dimensional quantum storage (green circles) and 5-dimensional quantum storage (red squares).